**5216** *Inorg. Chem.* **2009**, *48*, 5216–5223
DOI: 10.1021/ic900171u

Inorganic Chemistry
Article

# Neutron Diffraction, Electronic Band Structure, and Electrical Resistivity of $Mo_{3-x}Ru_xSb_7$

**Christophe Candolfi,*,†,⊥ Bertrand Lenoir,† Juliusz Leszczynski,† Anne Dauscher,† Janusz Tobola,‡ Simon J. Clarke,§ and Ron I. Smith‖**

†*Institut Jean Lamour, UMR 7198, Ecole Nationale Supérieure des Mines de Nancy, Parc de Saurupt, 54042 Nancy cedex, France,* ‡*Faculty of Physics and Applied Computer Science, AGH University of Science and Technology, 30-059 Krakow, Poland,* §*Department of Chemistry, University of Oxford, Inorganic Chemistry Laboratory, South Parks Road, Oxford OXI 3 QR, United Kingdom, and* ‖*ISIS Facility, Rutherford Appleton Laboratory, Chilton, Didcot, Oxon OX11 0QX, United Kingdom.* ⊥*Current address: Max-Planck-Institut für Chemische Physik fester Stoffe, Nöthnitzer Str. 40, 01187 Dresden, Germany*

Received January 27, 2009

Neutron diffraction experiments and Korringa−Kohn−Rostoker with coherent potential approximation electronic band structure calculations as well as electrical resistivity measurements have been performed on polycrystalline $Mo_{3-x}Ru_xSb_7$ samples for $0 \leq x \leq 1$. Neutron diffraction studies have been undertaken at room temperature and extended down to 4 K to get a better understanding of the crystalline structure modifications as the Ru content increases. Both structural and chemical characterizations have unambiguously revealed a solubility limit of the Ru atoms close to 0.8. Electronic band structure calculations have provided theoretical evidence of a progressive transition from a metalliclike state ($x = 0$) toward a semiconducting-like character as $x = 1$ is approached, although the solubility limit of Ru precludes a crossover to a semiconducting behavior. The theoretical prediction has been experimentally confirmed by low-temperature electrical resistivity measurements from 2 up to 350 K.

## I. Introduction

An efficient thermoelectric material requires a high value of the dimensionless figure of merit at a temperature $T$, ZT, defined as $ZT = \alpha^2 T/\lambda\rho$, where $\alpha$ stands for the Seebeck coefficient or thermopower, $\rho$ the electrical resistivity, and $\lambda$ the total thermal conductivity.[1,2] Though the overall improvement in the figure of merit had been marginal for more than 40 years (1950−1990), the situation radically changed in the early 1990s. Twenty years ago, a resurgence of interest in thermoelectricity occurred due to new theoretical guidelines predicting that nanostructured compounds as well as open crystalline structures could exhibit enhanced thermoelectric performance.[3−5] If the former idea is primarily based on quantum-confinement phenomena leading to variations of the density of states at the Fermi level favorable to achieving high thermopower values, the latter is related to the presence of cages in the crystalline structure where loose-bonded atoms can be inserted. These atoms can rattle about their equilibrium positions, giving rise to a resonant scattering mechanism and thus to a marked lowering of the lattice thermal conductivity. With these theoretical guidelines being followed, huge experimental efforts have been devoted to demonstrating the proof of principle. Exciting discoveries in low-dimensional structures such as quantum wells or quantum wires have been reported with the achievement of ZT values close to 2−3 near room temperature.[6−13] Encouraging results have also been obtained in cage compounds such as

*Author to whom correspondence should be addressed. E-mail: candolfi@mines.inpl-nancy.fr.

(1) Ioffe, A. F. *Physics of Semiconductors*; Academic Press: New York, 1960.
(2) Rowe, D. M. *CRC Handbook of Thermoelectrics*; CRC Press: Boca Raton, FL, 1995.
(3) Hicks, L. D.; Dresselhaus, M. S. *Phys. Rev. B* **1993**, *47*, 12727–12731.
(4) Hicks, L. D.; Dresselhaus, M. S. *Phys. Rev. B* **1993**, *47*, 16631–16634.
(5) Slack, G. A. In *CRC Handbook of Thermoelectrics*; CRC Press: Boca Raton, FL, 1995; Section D 34.
(6) Harman, T. C.; Taylor, P. J.; Walsh, M. P.; LaForge, B. E. *Science* **2002**, *297*, 2229–2232.
(7) Venkatasubramanian, R.; Siivola, E.; Colpitts, T.; O'Quinn, B. *Nature* **2001**, *413*, 597–602.
(8) Dresselhaus, M. S.; Chen, G.; Tang, M. Y.; Yang, R.; Lee, H.; Wang, D.; Ren, Z.; Fleurial, J. P. *Adv. Mater.* **2007**, *19*, 1043–1053.
(9) Hochbaum, A. I.; Chen, R.; Delgado, R. D.; Liang, W.; Garnett, E. C.; Najarian, M.; Majumdar, A.; Yang, P. *Nature* **2008**, *451*, 163–167.
(10) Boukai, A. I.; Bunimovich, Y.; Tahir-Kheli, J.; Yu, J. K.; Goddard, W. A.; Heath, J. R. *Nature* **2008**, *451*, 168–171.
(11) Sales, B. C.; Mandrus, D.; Williams, R. K. *Science* **1996**, *272*, 1325–1328.
(12) Uher, C. *Semiconductors and Semimetals*; Tritt, T. M., Ed.; Academic Press: New York, 2001; Vol *69*, p 139.
(13) Nolas, G. S.; Slack, G. A.; Schujman, S. B. *Semiconductors and Semimetals*; Tritt, T. M., Ed.; Academic Press: New York, 2001; Vol *69*, p 255.

 Published on Web 05/11/2009 

clathrates and skutterudites where ZT values exceeding unity have been discovered in the 500−800 K temperature range.[14−16]

Another interesting field of investigation pursued to discover high-efficiency thermoelectric materials is linked to the research of complex crystalline structures displaying a large number of atoms per unit cell. Among the different classes of compounds investigated up to now, Zintl phases have attracted great attention in the past five years from a thermoelectric point of view.[17] ZT values greater than unity have been obtained in the $Yb_{14}MnSb_{11}$ and $Yb_{14}Mn_{1-x}Zn_xSb_{11}$ compounds at high temperatures, near 1200 K, demonstrating their potential for high-temperature power generation.[18,19]

Another prospective family of Zintl phases, namely, $M_3T_7$ (with M = Nb, Mo, Tc, Re, Ru, Os, Ir, Co, Ni, Pd, and Pt and T = Sb, Te, As, Sn, Si, Al, Ga, Ge, In, Pb, and Tl) crystallizing in the cubic $Ir_3Ge_7$ structure type (space group *Im*3*m*, No. 229, 40 atoms per unit cell), has been recently considered as holding prime candidates for power generation near 1000 K.[20−22] These compounds crystallize in a body-centered cubic structure which is usually described as a three-dimensional arrangement of elementary building blocks formed by two antiprisms of T atoms.[21−24] Another useful crystallographic description can be obtained if we consider both the M and T sublattices. The M atoms form a body-centered cubic sublattice composed of octahedral structures similar to the $LaB_6$ crystalline structure (Figure 1).[25] The T1 atoms (T atoms are present on two inequivalent sites called T1 and T2) form truncated octahedra composed of six square faces and eight hexagonal faces (Figure 2a). The T2 atoms constitute dumbbell structures located perpendicularly at the center of each hexagonal face. The M and T sublattices are then assembled by positioning an M octahedral structure at the center of the T truncated octahedra (Figure 2b).

Among the different compounds which belong to this family, the $Re_3As_7$ and $Mo_3Sb_7$ compounds were found to be two interesting systems with potential for high ZT values.[20,21,23] Though only a few experimental studies have been devoted to the former compound up to now, the latter has been more deeply studied from both a fundamental and

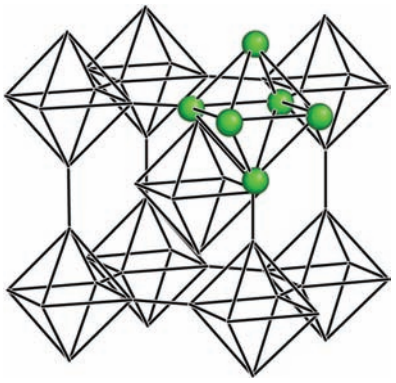

**Figure 1.** Cubic-centered M sublattice formed by octahedral structures in the $M_3T_7$ compounds.

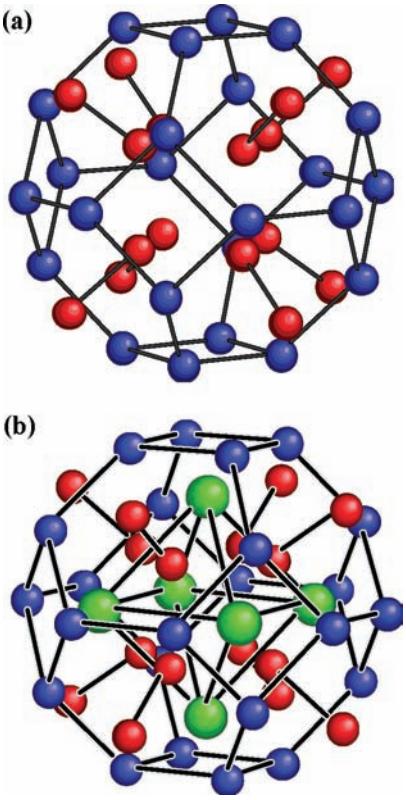


**Figure 2.** (a) Sublattice composed of T1 (in blue) and T2 (in red) atoms. (b) The M octahedral structure (in green) sits at the center of the T1 and T2 sublattice.

thermoelectric point of view.[26−28] Besides superconducting properties,[29−32] $Mo_3Sb_7$ exhibits exotic magnetic interactions leading to the opening of a spin gap in the spin excitation spectrum at $T^* = 53$ K.[26] One important feature in $Mo_3Sb_7$ and $Re_3As_7$ lies in the presence of an energy gap near the Fermi level, offering the opportunity to reach a

(14) Fleurial, J. P.; Borshchevsky, A.; Caillat, T.; Morelli, D. T.; Meisner, G. P. *Proceedings of the 15th International Conference on Thermoelectrics*; IEEE: Los Alamitos, CA, 1996; Vol *91*.
(15) Nolas, G. S.; Kaeser, M.; Littleton, R. T.; Tritt, T. M. *Appl. Phys. Lett*. **2000**, *77*, 1855–1857.
(16) Puyet, M.; Dauscher, A.; Lenoir, B.; Dehmas, M.; Stiewe, C.; Müller, E.; Hejtmanek, J. *J. Appl. Phys*. 2005, *97*, 083712 and references therein.
(17) Kauzlarich, S. M.; Brown, S. R.; Snyder, G. J. *Dalton Trans*. **2007**, 2099–2107.
(18) Brown, S. R.; Kauzlarich, S. M.; Gascoin, F.; Snyder, G. J. *Chem. Mater*. **2006**, *18*, 1873–1877.
(19) Brown, S. R.; Toberer, E. S.; Ikeda, T.; Cox, C. A.; Gascoin, F.; Kauzlarich, S. M.; Snyder, G. J. *Chem. Mater*. **2008**, *20*, 3412–3419.
(20) Dashjav, E.; Szczepenowska, A; Kleinke, H. *J. Mater. Chem*. **2002**, *12*, 345–349.
(21) Gascoin, F.; Rasmussen, J.; Snyder, G. J. *J. Alloys Compd*. **2007**, *427*, 324–329.
(22) Häussermann, U.; Elding-Ponten, M.; Svensson, C.; Lidin, S. *Chem.—Eur. J*. **1998**, *4*, 1007–1015.
(23) Soheilnia, N.; Xu, H.; Zhang, H.; Tritt, T. M.; Swainson, I.; Kleinke, H. *Chem. Mater*. **2007**, *19*, 4063–4068.
(24) Candolfi, C.; Lenoir, B.; Dauscher, A.; Tobola, J.; Clarke, S. J.; Smith, R. I. *Chem. Mater*. **2008**, *20*, 6556–6561.
(25) Ning, G.; Flemming, R. L. *J. Appl. Crystallogr*. **2005**, *38*, 757–759.
(26) Tran, V. H.; Miiller, W.; Bukowski, Z. *Phys. Rev. Lett*. **2008**, *100*, 137004.
(27) Candolfi, C.; Lenoir, B.; Dauscher, A.; Bellouard, C.; Hejtmanek, J.; Santava, E.; Tobola, J. *Phys. Rev. Lett*. **2007**, *99*, 037006.
(28) Candolfi, C.; Lenoir, B.; Dauscher, A.; Guilmeau, E.; Hejtmanek, J.; Tobola, J.; Wiendlocha, B.; Kaprzyk, S. *Phys. Rev. B* **2009**, *79*, 035114.
(29) Bukowski, Z.; Badurski, D.; Stepien-Damm, J.; Troc, R. *Solid State Commun*. **2002**, *123*, 283–286.
(30) Candolfi, C.; Lenoir, B.; Dauscher, A.; Hejtmanek, J.; Santava, E.; Tobola, J. *Phys. Rev. B* **2008**, *77*, 092509.
(31) Tran, V. H.; Hillier, A. D.; Adroja, D. T.; Bukowski, Z. *Phys. Rev. B* **2008**, *78*, 172505.
(32) Khasanov, R.; Klamut, P. W.; Shengelaya, A.; Bukowski, Z.; Savic, I. M.; Baines, C.; Keller, H. *Phys. Rev. B* **2008**, *78*, 014502.

semiconducting state. Band structure calculations have shown that adding two electrons to $Mo_3Sb_7$ or one hole to $Re_3As_7$ should lead to a crossover to semiconducting properties.[20,23] It should be emphasized that this scenario supposes rigidlike behavior of the electronic structure when electrons ($Mo_3Sb_7$) or holes ($Re_3As_7$) are added. These theoretical predictions have been experimentally investigated by substituting Sb with Te and As with Ge atoms.[20,23] One of the essential features of the former study is the existence of a solubility limit of Te which prevents the Fermi level from being driven into the gap. Nevertheless, as suggested by band structure calculations, these substitutions give rise to a shift of the Fermi level toward the valence and conduction band edges, respectively. Thus, both promising p-type and n-type materials, namely, $Mo_3Sb_{7-x}Te_x$ and $Re_3As_{7-x}Ge_x$, respectively, were found to present good thermoelectric properties at high temperatures.[21,23] These ZT improvements are mainly related to the Ge and Te concentration increases, which are accompanied by an enhancement of the Seebeck coefficient. Therefore, it is of prime interest to further investigate these systems to determine whether or not other substitutions that lead to a rigidlike behavior of the electronic structure are possible.

In this paper, we focus our attention on the $Mo_3Sb_7$ compound and demonstrate that Mo can be substituted by Ru. The variation of both the crystallographic and electronic structures with the Ru content constitutes the outstanding issues we address in the present paper. To study the former property, we carried out powder neutron diffraction experiments throughout the 4−300 K temperature range. Band structure calculations were performed to investigate how the density of states at the Fermi level evolves with $x$, that is, whether or not the variation of the electronic structure can be understood within a rigid band model. To provide further experimental evidence of a progressive metal−insulator transition as the Ru content increases predicted by our Korringa−Kohn−Rostoker with coherent potential approximation (KKR-CPA) calculations, low-temperature electrical resistivity measurements were also carried out.

## II. Experimental and Computational Details

**Synthesis.** Compounds of nominal composition $Mo_{3-x}Ru_xSb_7$ with $x = 0$, 0.25, 0.5, and 1 were prepared from stoichiometric amounts of pure Sb powders (5NPlus, 99.999%), Mo powders (Cerac, 99.999%), and Ru powders (Alfa Aesar, 99.99%). The reaction took place under a $He/H_2$ (95/5%) atmosphere in a sealed evacuated quartz ampule. The tubes were then transferred into a programmable furnace heated up to 750 °C for 10 days and then quenched in cold water. The resulting ingots were ground in an agate mortar into fine powders ($< 100$ $\mu$m) and further compacted into pellets in a steel die. To ensure good homogeneity of the samples, these pellets were annealed in a quartz ampule under a $He/H_2$ atmosphere at 750 °C for 7 days. The final products were powdered again and densified by hot-pressing in a graphite die in an argon atmosphere at 600 °C for 2 h under 51 MPa. The relative densities, defined as the ratio of the measured density (estimated from the geometrical dimensions and the weight of the cylindrical ingots) to the theoretical density, are 93, 98, 99, and 88% for the samples with nominal $x = 0$, 0.25, 0.5, and 1, respectively.

**Crystalline Structure and Chemical Analysis.** X-ray powder diffraction (XRD) was performed on the ground materials obtained before the sintering process. Experiments were conducted with a Siemens D500 diffractometer using Co Kα radiation and equipped with a curved primary beam monochromator and a linear positive sensitive detector. X-ray diffraction patterns were recorded in the $\theta-2\theta$ mode between 20° and 110° with a $2\theta$ step of 0.032° and a total counting time of 3 h. To obtain accurate lattice parameters, high-purity silicon ($a_0 = 5.4309$ Å) was added as an internal standard.

**Table 1.** Lattice Parameters of the Different $Mo_{3-x}Ru_xSb_7$ Compounds as Determined from X-Ray Diffraction

| chemical formula | lattice parameter (Å) |
|---|---|
| $Mo_3Sb_7$ | 9.568(8) |
| $Mo_{2.75}Ru_{0.25}Sb_7$ | 9.550(4) |
| $Mo_{2.5}Ru_{0.5}Sb_7$ | 9.524(9) |
| $Mo_{2.2}Ru_{0.8}Sb_7$ | 9.504(9) |
| $Mo_2RuSb_7$ | 9.500(8) |

No secondary phases could be detected in the $Mo_{2.75}Ru_{0.25}Sb_7$ and $Mo_{2.5}Ru_{0.5}Sb_7$ compounds, but a small concentration of $RuTe_2$ (~5 wt %) was evident in the XRD pattern of $Mo_2RuSb_7$ (nominal $x = 1$). These results not only demonstrate that molybdenum can be successfully substituted by ruthenium but also strongly suggest a solubility limit of Ru in the $Mo_3Sb_7$ crystalline structure. As we have already mentioned, similar behavior has been observed in the $Mo_3Sb_{7-x}Te_x$ system. A solubility limit of Te close to $x = 1.6$ was experimentally demonstrated, whereas a concentration as high as $x = 2$ should be required to achieve semiconducting properties.[20,21] To determine the actual chemical composition of $Mo_{2.75}Ru_{0.25}Sb_7$, $Mo_{2.5}Ru_{0.5}Sb_7$, and $Mo_2RuSb_7$, electron probe microanalysis studies (EPMA) have been performed with a CAMECA SX100.

These experiments have confirmed the XRD analyses, as they revealed that both the $Mo_{2.75}Ru_{0.25}Sb_7$ and $Mo_{2.5}Ru_{0.5}Sb_7$ compounds exhibit an excellent chemical homogeneity with a very good correlation between the actual and nominal compositions. This study has also corroborated the presence of secondary phases (mainly $RuTe_2$) in the sample of nominal composition $Mo_2RuSb_7$ and has revealed a solubility limit of the Ru atoms close to 0.8. Subsequently, we synthesized a phase-pure sample of $Mo_{2.2}Ru_{0.8}Sb_7$ at the Ru-rich limit for further experiments. Note that, for the sake of clarity and to distinguish from each other the pure sample at the solubility limit with $x = 0.8$ and the impure sample with nominal $x = 1$, the nominal compositions will always be used in the present paper.

The lattice parameters, $a$, of the different materials studied are summarized in Table 1. These results show a strong decrease of $a$, with the Ru content following Vegard's law (Figure 3). As we can appreciate, the lattice parameter of $Mo_{2.2}Ru_{0.8}Sb_7$ is slightly higher than that derived for $Mo_2RuSb_7$ (Table 1). We believe that this difference is linked to the experimental error of EPMA since a solubility limit of 0.85 instead of 0.8 would be in excellent agreement with Vegard's law (Figure 3).

**Neutron Diffraction.** To study in detail the evolution of the crystalline structure with the Ru content, we have carried out powder neutron diffraction measurements on the phase-pure samples. Data were collected on 3 g of $Mo_{2.75}Ru_{0.25}Sb_7$ and $Mo_{2.2}Ru_{0.8}Sb_7$ powders, contained in cylindrical vanadium cans, on the POLARIS time-of-flight diffractometer at the ISIS facility, Rutherford Appleton Laboratory, United Kingdom. $^3$He tube detector banks at 35° and 145° and a ZnS scintillation detector bank at 90° were used. This allows us to access an overall $d$-spacing spanning the range $0.3 \leq d \leq 8$ Å. Data were acquired at room temperature for the $Mo_{2.75}Ru_{0.25}Sb_7$ and $Mo_{2.2}Ru_{0.8}Sb_7$ compounds as well as at low temperatures (220, 150, 80, and 4 K) for the latter. To compare the crystallographic data of the Ru-substituted samples with those of the parent compound, additional experiments at the same temperatures have been performed on $Mo_3Sb_7$. All of these measurements were acquired for 2 h at all temperatures and made for an integrated proton current at the production target of 200 $\mu$A h. Rietveld refinements were carried out on the data collected on

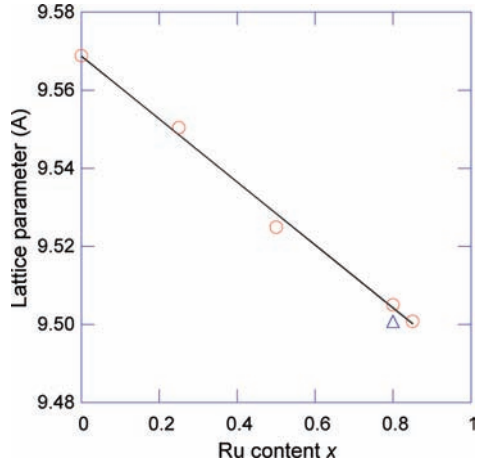


**Figure 3.** Lattice parameter variation of the $Mo_{3-x}Ru_xSb_7$ system as a function of the actual Ru content, determined from X-ray powder diffraction. The ○ symbols refer to the lattice parameters of the $x = 0$, $x = 0.25$, $x = 0.5$, and $x = 0.8$ samples. The △ symbol stands for the lattice parameter of the impure $x = 1$ sample, which suggests a solubility limit of Ru of ~0.85 assuming Vegard's law is obeyed. The solid line represents the best fit to the data.

the 145° bank (backscattering detectors) using the Fullprof program.[33] The relevant crystallographic details from the neutron diffraction analysis are summarized in Table 2.

**Electronic Band Structure Calculations.** Electronic structure calculations of the $Mo_{3-x}Ru_xSb_7$ system ($0 \leq x \leq 1$) were performed using the Korringa−Kohn−Rostoker[34−36] method with the coherent potential approximation, where the chemical disorder has been treated as a random atom distribution on the Mo site. The self-consistent crystal potential of the muffin-tin form was constructed within the local density approximation, applying the Perdew−Wang formula for the exchange-correlation part. For well-converged charges and potentials, total and partial densities of states were computed. Experimental lattice constants and positional parameters of Mo (12e) and Sb2 (16f) atoms derived from our neutron diffraction analysis were used in these calculations.

**Electrical Resistivity Measurements.** Electrical resistivity measurements were carried out over the temperature range 2−350 K using an ac transport measurement system option (PPMS-Quantum Design). This study was realized on parallelepipedic-shaped samples cut from the hot-pressed ingots with a diamond wire saw to typical dimensions of $2 \times 2 \times 10$ mm$^3$. Ohmic contacts to the samples were made with fine copper wires carefully attached using a tiny amount of silver paint.

## III. Results and Discussion

**Neutron Diffraction Analysis.** The refinements against data on $Mo_3Sb_7$ were performed using the published XRD data as a starting model. This compound undergoes a structural deformation below $T^* = 53$ K, where a spin gap opens in the spin excitation spectrum.[37,38] Low-temperature XRD investigations on polycrystalline samples shed light on this structural symmetry breaking by suggesting a cubic-to-tetragonal transformation (space group $I4/mmm$). Thus, the lattice parameter of the cubic structure, $a$, splits into two distinct parameters $a$ and $c$, with $a < c$, without any drastic changes in the lattice volume. The amplitude of the deformation was found to be very slight, as typified by an $a/c$ ratio close to unity ($a/c \sim 1.002$ at 10 K).[38] However, these experiments did not rule out possibilities of a crystal lattice with lower symmetry nor a long-period modulated lattice. XRD measurements on high-quality single crystals are therefore mandatory to definitively settle this issue. Such slight transformation could not be resolved in the present neutron diffraction experiments performed on a medium-resolution instrument, and hence, we refined the 4 K pattern by considering the cubic phase displayed by $Mo_3Sb_7$ above $T^*$. For each temperature investigated, the refinement easily converged to a fully ordered atom arrangement with respect to the site distribution of Mo and Sb atoms and, hence, leads to good agreement factors (Table 3). The relevant crystallographic parameters are listed in Table 4. The anisotropic thermal displacement parameters as well as selected bond lengths are provided in the Supporting Information. The lattice parameter obtained at 300 K is in very good agreement with those found in previous works.[24] Interestingly, the isotropic atomic displacement parameter of the Mo atoms is significantly lower than those of the Sb1 and Sb2 atoms. This behavior is likely due to the position of the Mo atoms inside the antiprisms. From the temperature dependences of the lattice parameter and ADP values, valuable information on $Mo_3Sb_7$ can be inferred. As shown in Figure 4, the lattice parameter decreases linearly down to 150 K and then tends to saturate as the temperature is decreased to 4 K. The thermal dilatation coefficient $\alpha_T$ can be derived from the temperature dependence of the lattice parameter using

$$\alpha_T = \left(\frac{1}{V}\frac{\partial V}{\partial T}\right)_p = \left(\frac{3}{a}\frac{\partial a}{\partial T}\right)_p \quad (1)$$

At 300 K, $\alpha_T$ is equal to $25.10^{-6}$ K$^{-1}$. Both this value and the temperature evolution of the lattice parameter are similar to those observed for other thermoelectric materials, such as skutterudites, for instance.[39] When the temperature dependence of the isotropic thermal displacement parameters is used, the Debye temperature,

**Table 2.** Crystallographic Data from Neutron Diffraction Experiments on the $Mo_3Sb_7$ and $Mo_{3-x}Ru_xSb_7$ Compounds ($x = 0.25$ and 0.8)

| | $Mo_3Sb_7$ | $Mo_{2.75}Ru_{0.25}Sb_7$ | $Mo_{2.2}Ru_{0.8}Sb_7$ |
|---|---|---|---|
| fw (g mol$^{-1}$) | 1140.1 | 1141.4 | 1144.2 |
| $T$ (K) | 298 | 298 | 298 |
| space group | *Im*3*m* | *Im*3*m* | *Im*3*m* |
| cell dimensions a (Å) | 9.5715 | 9.5483 | 9.5073 |
| $V$ (Å$^3$) | 876.90 | 870.52 | 859.36 |
| no. of formula units per cell | 4 | 4 | 4 |
| calcd density (g.cm$^{-3}$) | 8.64 | 8.71 | 8.85 |
| TOF range ($\mu$s) | 2000−19000 | 2000−19000 | 2000−19000 |

(33) Rodriguez-Carvajal, J. *Abstracts of the Satellite Meeting on Powder Diffraction of the XV Congress of the IUCr*; International Union of Crystallography: Chester, England, 1990; pp 127−128.
(34) Korringa, J. *Physica* **1947**, *13*, 392.
(35) Kohn, W.; Rostoker, N. *Phys. Rev.* **1954**, *94*, 1111–1120.
(36) Bansil, A.; Kaprzyk, S.; Mijnarends, P. E.; Tobola, J. *Phys. Rev. B* **1999**, *60*, 13396–13412.
(37) Koyama, T.; Yamashita, H.; Takahashi, Y.; Kohara, T.; Watanabe, I.; Tabata, Y.; Nakamura, H. *Phys. Rev. Lett.* **2008**, *101*, 126404.
(38) Koyama, T.; Yamashita, H.; Kohara, T.; Tabata, Y.; Nakamura, H. *Mater. Res. Bull.* **2009**, *44*, 1132–1135.
(39) Caillat, T.; Fleurial, J. P.; Borshchevski, A. *J. Cryst. Growth* **1996**, *166*, 722–726.

**Table 3.** Agreement Factors of the Rietveld Analysis of the $Mo_{3-x}Ru_xSb_7$ Neutron Diffraction Patterns for $x = 0$, 0.25, and 0.8

| | $x = 0$ | | | | | $x = 0.25$ | $x = 0.8$ | | | | |
|---|---|---|---|---|---|---|---|---|---|---|---|
| sample | 300 K | 220 K | 150 K | 80 K | 4 K | 300 K | 300 K | 220 K | 150 K | 80 K | 4 K |
| $R_p$ | 1.22 | 1.28 | 1.40 | 1.43 | 1.46 | 3.01 | 1.55 | 1.62 | 1.65 | 1.72 | 1.71 |
| $R_{wp}$ | 0.92 | 1.00 | 1.07 | 1.13 | 1.16 | 2.86 | 1.14 | 1.17 | 1.23 | 1.23 | 1.27 |
| $R_{exp}$ | 0.70 | 0.70 | 0.71 | 0.71 | 0.71 | 1.24 | 0.83 | 0.83 | 0.83 | 0.83 | 0.83 |
| $\chi^2$ | 1.70 | 2.00 | 2.29 | 2.57 | 2.65 | 5.34 | 1.88 | 1.98 | 2.20 | 2.18 | 2.31 |

**Table 4.** Atomic Positions and Isotropic Displacement Parameters (given in $Å^2$) of $Mo_3Sb_7$

| atom | site | $x$ | $y$ | $z$ | $B_{iso}$ ($Å^2$) | occupancy (%) |
|---|---|---|---|---|---|---|
| | | | 300 K | | | |
| Mo | 12e | 0.343(5) | 0 | 0 | 0.31(2) | 100 |
| Sb1 | 12d | 0.25 | 0 | 0.5 | 0.44(7) | 100 |
| Sb2 | 16f | 0.162(3) | 0.162(3) | 0.162(3) | 0.45(6) | 100 |
| | | | 220 K | | | |
| Mo | 12e | 0.343(5) | 0 | 0 | 0.24(8) | 100 |
| Sb1 | 12d | 0.25 | 0 | 0.5 | 0.34(7) | 100 |
| Sb2 | 16f | 0.162(4) | 0.162(4) | 0.162(4) | 0.35(2) | 100 |
| | | | 150 K | | | |
| Mo | 12e | 0.343(4) | 0 | 0 | 0.20(2) | 100 |
| Sb1 | 12d | 0.25 | 0 | 0.5 | 0.26(5) | 100 |
| Sb2 | 16f | 0.162(3) | 0.162(3) | 0.162(3) | 0.25(9) | 100 |
| | | | 80 K | | | |
| Mo | 12e | 0.342(6) | 0 | 0 | 0.16(6) | 100 |
| Sb1 | 12d | 0.25 | 0 | 0.5 | 0.18(9) | 100 |
| Sb2 | 16f | 0.161(6) | 0.161(6) | 0.161(6) | 0.17(3) | 100 |
| | | | 4 K | | | |
| Mo | 12e | 0.343(2) | 0 | 0 | 0.15(1) | 100 |
| Sb1 | 12d | 0.25 | 0 | 0.5 | 0.15(2) | 100 |
| Sb2 | 16f | 0.162(2) | 0.162(2) | 0.162(2) | 0.11(9) | 100 |

$\theta_D$, can be estimated using the formalism developed by Willis and Pryor[40]

$$\bar{B}_{iso} = \frac{6nh^2}{Mk_B\theta_D}\left[\frac{\Phi\left(\frac{\theta_D}{T}\right)}{\frac{\theta_D}{T}} + \frac{1}{4}\right] \quad (2)$$

with $\Phi(x) = {}^1/_x\int_0^x {}^y/_{e^y - 1}\,dy$. In eq 2, $\overline{B}_{iso}$ stands for the mean value of the thermal displacement parameter of both Mo and Sb atoms, $M$ is the molar weight of the $Mo_3Sb_7$ compound, $n$ is the number of atoms per unit cell, $h$ is the Planck constant, and $k_B$ is the Boltzmann constant. From the crystallographic data summarized in Table 4 and with $n = 40$ and $M = 1140.14$ g mol$^{-1}$, we get $\theta_D \sim 300$ K, in very good agreement with the values derived from ultrasound velocity analysis ($\theta_D \sim 285$ K) and low-temperature specific heat measurements ($\theta_D \sim 310$ K).[27,28]

In the following part, we turn our attention to the variations of the crystallographic parameters as the Ru content increases.

Figure 5 illustrates the refinement of the neutron time-of-flight diffraction pattern of $Mo_{2.75}Ru_{0.25}Sb_7$ obtained at 300 K. The crystallographic parameters of $Mo_3Sb_7$ determined at 300 K were used as a starting model. Because of similar scattering lengths (Mo = 6.715 fm and Ru = 7.03 fm), atomic displacement parameters and site occupancy factors were not simultaneously refined. Thus, the Ru content has been fixed to its nominal value. This hypothesis seems reasonable considering that the sample is single-phase and that EPMA measurements have suggested phase homogeneity. The model then easily converged to good agreement factors (Table 3). No ordering of the Ru atoms on the Mo site could be evidenced neither by neutron diffraction nor by XRD experiments, suggesting that Ru atoms randomly occupy the Mo site. The key parameters of the crystalline structure are given in Table 5. The lattice parameter is in very good agreement with that determined by X-ray diffraction. The decrease of this characteristic is, as expected, related to a decrease of the different bond lengths of the structure (Table 6). An exception to this behavior is related to the Mo−Mo bond lengths, which decrease initially and then increase for higher Ru concentrations. However, it must be emphasized that this exception depends on the lattice parameter value. The value derived from the X-ray diffraction experiment would lead to lower Mo−Mo bond lengths, which will therefore progressively increase with the Ru content (the behavior of all other bond lengths with $x$ will remain unchanged).

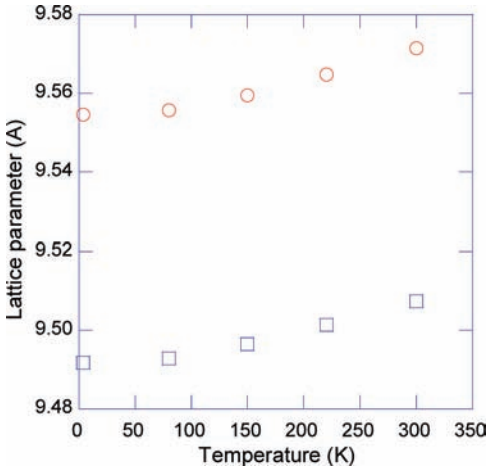


**Figure 4.** Temperature dependence of the lattice parameters of $Mo_3Sb_7$ (○) and $Mo_{2.2}Ru_{0.8}Sb_7$ (□) in the 4−300 K temperature range obtained from neutron diffraction experiments.

The refinement of the structure of $Mo_{2.2}Ru_{0.8}Sb_7$ was performed using the crystallographic parameters of the $x = 0.25$ sample as the starting model and by following the same approach. It must be emphasized that the low-temperature deformation that characterizes the $Mo_3Sb_7$ compound no longer exists in the Ru substituted samples. Convergence was rapidly attained and led to good agreement factors at all temperatures (Table 3).

(40) Willis, B. T. M.; Pryor, A. W. *Thermal Vibrations in Crystallography*; Cambridge University Press: London, 1975.

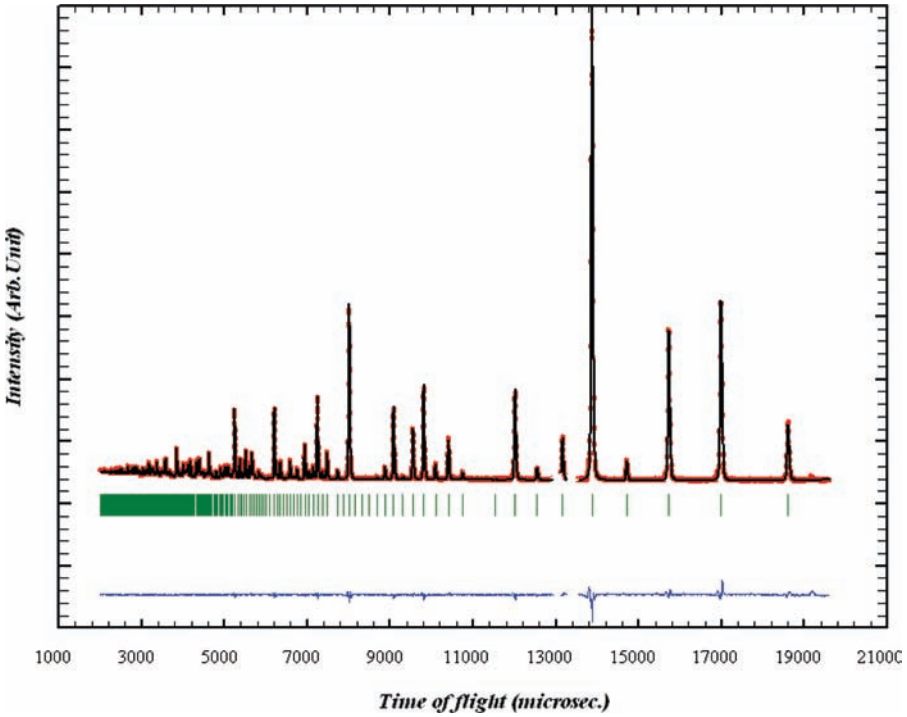


**Figure 5.** Rietveld refinement of the neutron diffraction pattern of the $Mo_{2.75}Ru_{0.25}Sb_7$ compound at 300 K. The lack of data near 13000 $\mu$s corresponds to additional peaks coming from the vanadium can and the cryostat used for these experiments.

**Table 5.** Relevant Crystallographic Parameters of the $Mo_{2.75}Ru_{0.25}Sb_7$ Compound

| atom | site | $x$ | $y$ | $z$ | $B_{iso}$ (Å$^2$) | occupancy (%) |
|---|---|---|---|---|---|---|
| Mo | 12e | 0.343(3) | 0 | 0 | 0.26(2) | 91.7 |
| Ru | 12e | 0.343(3) | 0 | 0 | 0.26(2) | 8.3 |
| Sb1 | 12d | 0.25 | 0 | 0.5 | 0.44(6) | 100 |
| Sb2 | 16f | 0.162(4) | 0.162(4) | 0.162(4) | 0.45(1) | 100 |

The crystallographic data are summarized in Table 7. The anisotropic thermal displacement parameters and selected bond lengths for each temperature investigated can be found in the Supporting Information file. The low-temperature dependence of both the lattice parameter and ADP values allows us to determine the thermal dilatation coefficient and the Debye temperature, respectively (Figure 4). Using eqs 1 and 2, we get $\alpha_T \sim 23.10^{-6}$ K$^{-1}$ and $\theta_D \sim 320$ K. As expected, these values are very close to those obtained for the parent compound since Mo and Ru atoms display close molar masses and atomic radii.

Soheilnia et al.[41] have suggested that lowering the lattice thermal conductivity could be possible in $Mo_3Sb_7$ by insertion of small cations into the cubic voids of the crystalline structure formed by the Sb2 atoms. It is interesting to underline that the presence of ruthenium leads to a decrease of the Sb2−Sb2 bonds and, as a consequence, to a decrease of the size of the cubes. Hence, if such insertions are possible in $Mo_3Sb_7$, this structural characteristic seems to strongly restrict this field of investigation to optimize the thermolectric properties of these Ru-substituted compounds.

The insertion of Ru atoms in the $Mo_3Sb_7$ crystalline structure should lead to a shift of the Fermi level toward the valence band edge since this substitution is expected to bring two additional electrons per Ru atom. This picture implies "rigid" behavior of the electronic structure as the Ru content increases. To glean what happens to the band structure when the Ru fraction spans the range $0 \leq x \leq 1$, we have undertaken electronic band structure calculations.

**Table 6.** Selected Interatomic Distances (Å) of $Mo_3Sb_7$, $Mo_{2.75}Ru_{0.25}Sb_7$, and $Mo_{2.2}Ru_{0.8}Sb_7$ at 300 K

| | $Mo_3Sb_7$ | $Mo_{2.75}Ru_{0.25}Sb_7$ | $Mo_{2.2}Ru_{0.8}Sb_7$ |
|---|---|---|---|
| Mo−Mo | 2.995(1) ×1 | 2.991(4) ×1 | 2.998(2) ×1 |
| Mo−Sb1 | 2.822(9) ×4 | 2.816(9) ×4 | 2.810(1) ×4 |
| Mo−Sb2 | 2.799(7) ×4 | 2.792(1) ×4 | 2.775(8) ×4 |
| Sb2−Sb2 | 2.907(5) ×1 | 2.895(5) ×1 | 2.871(2) ×1 |
| Sb2−Sb2 | 3.107(1) ×3 | 3.102(4) ×3 | 3.096(1) ×3 |
| Sb1−Sb1 | 3.384(0) ×4 | 3.375(8) ×4 | 3.361(3) ×4 |
| Sb1−Sb2 | 3.683(1) ×8 | 3.673(2) ×8 | 3.655(1) ×8 |

**Electronic Structure Calculations.** Figure 6 illustrates the total density of states at the Fermi level, $N(E_F)$, as a function of the Ru content. As this figure shows, the increase of the ruthenium content dramatically alters $N(E_F)$, which decreases with $x$. For $x = 1$, two electrons are added and all contributions vanish: the Fermi level enters the gap, and a crossover from the metallic state to a semiconducting regime occurs. In addition, this evolution supports the idea of a rather "rigid" behavior of the valence bands. Further evidence for this viewpoint is delivered by the variations of $N(E_F)$ as a function of the energy, displayed for several Ru contents in Figure 7. Besides the shift of the Fermi level, these data highlight the slight modifications undergone by the valence bands as $x$ increases.

Even though our experimental data have revealed a solubility limit of Ru lower than the required value to change the nature of the conduction process, the increase of the Ru content should lead to a decrease of $N(E_F)$, and as a consequence, a decrease of the carrier concentration

(41) Soheilnia, N.; Dashjav, E.; Kleinke, H. *Can. J. Chem.* **2003**, *81*, 1157–1163.

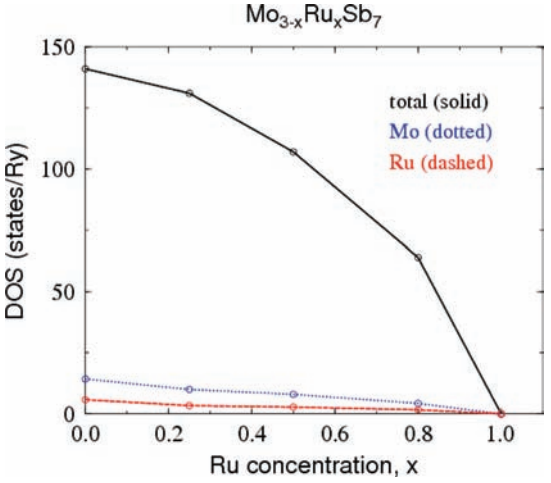


**Figure 6.** Evolution of the total density of states at the Fermi level as a function of the Ru content. The partial densities of states of the Mo and Ru atoms are also illustrated.

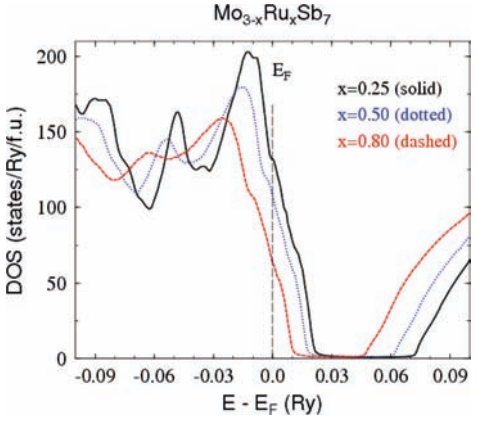


**Figure 7.** Valence band variation as a function of the Ru content in $Mo_{3-x}Ru_xSb_7$.

**Table 7.** Atomic Positions and Isotropic Displacement Parameters (given in Å$^2$) of $Mo_{2.2}Ru_{0.8}Sb_7$

| atom | site | $x$ | $y$ | $z$ | $B_{iso}$ (Å$^2$) | occupancy (%) |
|---|---|---|---|---|---|---|
| | | | 300 K | | | |
| Mo−Ru | 12e | 0.342(3) | 0 | 0 | 0.27(3) | 73.34/26.66 |
| Sb1 | 12d | 0.25 | 0 | 0.5 | 0.35(8) | 100 |
| Sb2 | 16f | 0.162(8) | 0.162(8) | 0.162(8) | 0.36(2) | 100 |
| | | | 220 K | | | |
| Mo−Ru | 12e | 0.342(3) | 0 | 0 | 0.20(4) | 73.34/26.66 |
| Sb1 | 12d | 0.25 | 0 | 0.5 | 0.26(8) | 100 |
| Sb2 | 16f | 0.162(8) | 0.162(8) | 0.162(8) | 0.27(2) | 100 |
| | | | 150 K | | | |
| Mo−Ru | 12e | 0.342(3) | 0 | 0 | 0.15(6) | 73.34/26.66 |
| Sb1 | 12d | 0.25 | 0 | 0.5 | 0.19(6) | 100 |
| Sb2 | 16f | 0.162(8) | 0.162(8) | 0.162(8) | 0.18(8) | 100 |
| | | | 80 K | | | |
| Mo−Ru | 12e | 0.342(1) | 0 | 0 | 0.12(6) | 73.34/26.66 |
| Sb1 | 12d | 0.25 | 0 | 0.5 | 0.12(7) | 100 |
| Sb2 | 16f | 0.162(7) | 0.162(7) | 0.162(7) | 0.12(2) | 100 |
| | | | 4 K | | | |
| Mo−Ru | 12e | 0.342(1) | 0 | 0 | 0.11(3) | 73.34/26.66 |
| Sb1 | 12d | 0.25 | 0 | 0.5 | 0.09(6) | 100 |
| Sb2 | 16f | 0.162(7) | 0.162(7) | 0.162(7) | 0.09(5) | 100 |

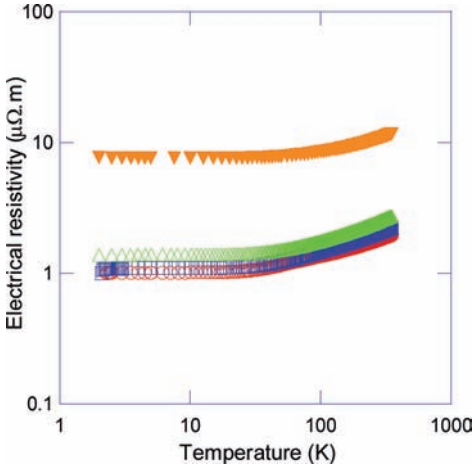


**Figure 8.** Temperature dependence of the electrical resistivity of the $Mo_{3-x}Ru_xSb_7$ compounds for $x = 0$ (○), 0.25 (□), 0.5 (△), and 1 (▼).

should arise. This picture can be experimentally investigated by measuring the electrical resistivity of the $Mo_{2.75}Ru_{0.25}Sb_7$, $Mo_{2.5}Ru_{0.5}Sb_7$, and $Mo_2RuSb_7$ compounds.

**Electrical Resistivity Measurements.** Figure 8 shows the temperature dependence of the electrical resistivity in the 2−350 K temperature range. The $x = 0$, 0.25, and 0.5 samples display metal-like character (positive $d\rho/dT$) in the whole temperature range, whereas the $x = 1$ sample shows similar behavior only above 15 K. These results unequivocally show that the Ru concentration is too low to achieve a changeover to semiconducting behavior. As can be clearly noticed, the electrical resitivity values increase with the Ru fraction. The strong difference between the $x = (0, 0.25\ 0.5)$ and $x = 1$ samples is only partially related to the lower relative density of the latter. Actually, as evidenced by our KKR-CPA outcomes displayed in Figure 6, the decrease of $N(E_F)$ is more pronounced for $x > 0.5$. Thus, we can expect a more dramatic decrease of the carrier concentration, leading to a higher drop in the electrical resistivity values. These results strongly corroborate our theoretical statements: the variation of the electrical resistivity mainly depends on the carrier density, which is controlled by the position of the Fermi level. Actually, magnetotransport measurements performed on these compounds, and described in detail elsewhere,[42] show that the Hall carrier mobility, $\mu_H$, does not exhibit strong variations with the Ru content ($\mu_H$ is on the order of a few cm$^2$ V$^{-1}$ s$^{-1}$). Thus, the electrical resistivity increase is intimately related to the decrease of the carrier density, which, in turn, is related to the decrease of $N(E_F)$. Therefore, even though a semiconducting state is not reached, these measurements provide strong evidence of a progressive metal−insulator transition as the Ru content increases.

## Conclusion

In this paper, we have discussed the evolution of both the crystalline and electronic structure of polycrystalline $Mo_{3-x}Ru_xSb_7$ compounds as the Ru content increases. Chemical and structural characterizations based on EPMA

(42) Candolfi, C.; Lenoir, B.; Leszczynski, J.; Dauscher, A.; Guilmeau, E. *J. Appl. Phys.* **2009**, *105*, 083701.

and XRD have revealed the existence of a solubility limit of ruthenium in $Mo_3Sb_7$, which we have determined to correspond to $x \sim 0.8$. Neutron diffraction experiments down to 4 K shed some light on the essential feature of the crystal structure, that is, a strong decrease of the lattice parameter when $x$ spans the range $0 \leq x \leq 1$. Band structure calculations have shown that an increase of the Ru fraction is associated with a decrease of the total density of states at the Fermi level up to $x = 1$. At this concentration, a metal−insulator transition is expected. The main result of our calculations lies in the rigidlike behavior of the electronic structure by adding electrons. Such variation is coherent with an enhancement of the electrical resistivity when $x$ increases. These measurements also clearly demonstrate that a change-over to semiconducting properties does not occur due to the solubility limit of ruthenium. Low-temperature transport property measurements will provide a deeper insight into the microscopic mechanisms which govern the electrical and thermal conduction processes, while high-temperature experiments will help to assess properly the thermoelectric potential of these new compounds.

**Acknowledgment.** C.C. greatly thanks M. Amiet and P. Maigné, and acknowledges the financial support of the DGA (Délégation Générale pour l'Armement, Ministry of Defense, France) and the European Network of Excellence CMA (Complex Metallic Alloys). J.T. acknowledges the support of the Polish Ministry of Science and Higher Education (Grant No. N202-2104-33). Dr. C. Bellouard is warmly thanked for her assistance in low-temperature electrical measurements.

**Supporting Information Available:** Four tables of the temperature dependence of the anisotropic thermal displacement parameters and selected bond lengths of $Mo_3Sb_7$ and $Mo_{2.2}Ru_{0.8}Sb_7$. This material is available free of charge via the Internet at http://pubs.acs.org.